

**Nassim A. Samad<sup>1</sup>**

Mem. ASME

Department of Mechanical Engineering,  
University of Michigan,  
Ann Arbor, MI 48109  
e-mail: nassimab@umich.edu

**Boyun Wang**

Department of Mechanical Engineering,  
University of Michigan,  
Ann Arbor, MI 48109  
e-mail: bywang@umich.edu

**Jason B. Siegel**

Department of Mechanical Engineering,  
University of Michigan,  
Ann Arbor, MI 48109  
e-mail: siegeljb@umich.edu

**Anna G. Stefanopoulou**

Professor  
Fellow ASME  
William Clay Ford Professor of Manufacturing  
Mechanical Engineering,  
Automotive Research Center,  
University of Michigan,  
Ann Arbor, MI 48109  
e-mail: annastef@umich.edu

# Parameterization of Battery Electrothermal Models Coupled With Finite Element Flow Models for Cooling

*Developing and parameterizing models that accurately predict the battery voltage and temperature in a vehicle battery pack are challenging due to the complex geometries of the airflow that influence the convective heat transfer. This paper addresses the difficulty in parameterizing low-order models which rely on coupling with finite element simulations. First, we propose a methodology to couple the parameterization of an equivalent circuit model (ECM) for both the electrical and thermal battery behavior with a finite element model (FEM) for the parameterization of the convective cooling of the airflow. In air-cooled battery packs with complex geometries and cooling channels, an FEM can provide the physics basis for the parameterization of the ECM that might have different convective coefficients between the cells depending on the airflow patterns. The second major contribution of this work includes validation of the ECM against the data collected from a three-cell fixture that emulates a segment of the pack with relevant cooling conditions for a hybrid vehicle. The validation is performed using an array of thin film temperature sensors covering the surface of the cell. Experiments with pulsing currents and drive cycles are used for validation over a wide range of operating conditions (ambient temperature, state of charge, current amplitude, and pulse width).*

[DOI: 10.1115/1.4035742]

## 1 Introduction

Growing use and acceptance of lithium-ion batteries in automotive and high-power applications are the result of lowered battery cost and increased system safety. Accurate mathematical battery models are necessary to define the safe operating limits, both thermal and electrochemical. Without accurate models, battery performance is sacrificed due to the overlying conservative bounds. The battery temperature must be regulated during high power operation due to internal heating of the cell. If the cell temperature rises above the breakdown temperature of the electrolyte or solid-electrolyte interface, thermal runaway could occur [1]. Researchers have focused on analyzing and understanding the behavior of lithium-ion cells as a means to overcome these obstacles. Bernardi et al. [2] proposed a general energy balance for batteries to predict the temperature. Successive researchers have attempted different approaches to modeling the thermal and electrical behavior of lithium-ion batteries. Physics-based models [3–5], which solve the governing equations of lithium-ion transport in the cell, can predict microscopic level behavior and performance, but require large computational power to solve the associated differential equations. Other models, which are more adequate for control-oriented purposes such as in the battery management system (BMS) of a vehicle, employ electrical circuit elements [6–15] to model the physical responses of the battery. These equivalent circuit models (ECMs) models are relatively easy to parameterize and are sufficiently accurate which justifies their use in a BMS.

Equivalent circuit models have been applied to cylindrical and prismatic cells. In cylindrical cells, ECM models that predict internal cell temperatures can be used to limit power [16] and regulate battery states. Gao at al. [11] formulated a single RC equivalent circuit model with temperature and state of discharge (SOD) dependent open circuit voltage (OCV), coupled with a “bulk” thermal model that characterizes the whole battery as one uniform temperature. Perez et al. [12] expanded on Gao’s model to include a two-state thermal model (surface and core) coupled with a double RC equivalent circuit model with temperature and state of charge-dependent parameters. Smith et al. [14] used finite-volume methods to model the temperature distributions along with a representative equivalent circuit model.

Prismatic cells can be physically packaged more efficiently than cylindrical cells. These cells are usually used in consumer electronics, like phones and laptops, and in hybrid electric vehicles such as the Ford Fusion Hybrid and the Toyota Prius Hybrid. However, they are harder to model than cylindrical cells due to their slightly more complex geometry. Many techniques were proposed in the literature for modeling the thermal behavior of prismatic cells [7,13,15,17–21]. Wang and coworkers [17] considered different thermal models and studied the computational efficiency and accuracy of these models. Inui et al. [18] considered the effect of the cross-sectional area of a prismatic battery on the temperature distributions within that battery. Gualous and coworkers [19] developed a new thermal parameter estimation tool using a first-order Cauer thermal model, and investigated the behavior of a battery under abuse conditions. Other more recent models have presented coupled electrothermal models that can predict temperature distributions in a prismatic cell [7,13,20]. In particular, coupled electrothermal models with distributed equivalent circuits [7,13] have been able to capture the local dynamics of prismatic cells and observe the local variations in temperature, current, and SOC.

<sup>1</sup>Corresponding author.

Contributed by the Dynamic Systems Division of ASME for publication in the JOURNAL OF DYNAMIC SYSTEMS, MEASUREMENT, AND CONTROL. Manuscript received October 6, 2015; final manuscript received December 19, 2016; published online May 9, 2017. Assoc. Editor: Beshah Ayalew.

Most of the prior work on ECM parameterization has not addressed vehicle battery pack conditions, especially, in terms of airflow parameterization. Due to the complex geometries and airflow patterns in a vehicle battery pack, a methodology to parameterize the ECM airflow parameters and hence the heat convection such that they could capture the influence of the cooling system is required. This could be achieved by coupling the parameterization of the ECM with an finite element model (FEM) that reproduces the geometry of the pack. Also, the ECMS present in the literature have performed validation under a limited set of operating conditions that fail to span the different operating conditions relevant for automotive applications. Some of these models present equivalent circuit models with validated electrical behavior only but not thermal behavior [8–10]. Murashko et al. [7] validated their model against only different C-rates and SOC ranges. Perez et al. [12] performed validation only against one drive cycle at an ambient temperature of 25 °C. Samba et al. [19] on the other hand, validated their model thermally against different C-rates but did not validate the electrical behavior.

This paper thus presents two main contributions. The first is a co-simulation method that couples the parameterization of an ECM with an FEM for thermal prediction under natural and forced convection. The ECM is first tuned given no flow conditions. Then, using the thermal properties identified, the ECM is coupled with an FEM offline to tune the heat transfer coefficient for a given coolant flow. The second contribution is the validation of the ECM against a wide range of operating conditions (ambient temperature, state of charge, current amplitude, and pulse width) for an encased prismatic cell operating in a fixture that replicates the airflow and hence the cooling that cells will experience if they were contained in a pack.

In what follows, a methodology is presented that couples the electrical and thermal behavior of a prismatic cell which includes local current, states of charge with average flow conditions, and temperature distributions. This model combines aspects of flow prediction and the achieved convection from FEMs with simple one or two state electrothermal models. A three-dimensional (3D) thermal network with surface nodes and core nodes that lump the average properties of the jelly roll inside the battery is coupled to a two-dimensional (2D) electrical model with distributed double

RC equivalent circuits at each core node. The model assumes infinite conduction in the electrodes which means that all the core nodes are electrically connected in parallel. This first-order assumption is valid for low current rates and allows for easier parameterization of the local electrical nodes. The distributed nodal mesh is then validated with new thin film sensors with 0.5 °C accuracy. The sensors are mounted on the surface of the cell and placed into a fixture that replicates the pack conditions with forced air cooling across the cell. The model is parameterized by coupling with a high fidelity FEM which allows for identifying flow velocities over the surface of the cell without the need for flow sensors. Unlike simple one and two-state models, this distributed temperature model can be used to predict the spatial temperature distributions, while maintaining a fast computational approach. The model was validated against different drive cycles ( $T_{amb} \in [-5, 25]^\circ\text{C}$ ) and pulse experiments at different temperatures ( $T_{amb} \in [-5, 10, 25]^\circ\text{C}$ ), SOC  $\in [25, 50, 75]\%$ , current amplitudes  $\in [25, 50] \text{ A}$ , and pulse width  $\in [5, 50] \text{ s}$ . The resulting root-mean-square error (RMSE) on voltage in all cases was less than 20 mV and on average temperature less than 0.5 °C, except at  $-5^\circ\text{C}$ , where the RMSE on temperature was 1.3 °C despite the good electric accuracy (RMSE on voltage was less than 15 mV).

## 2 Battery Modeling

In HEVs built around the existing ICE platform, the battery system is typically packaged into the available space, placing constraints on the routing of the coolant into and out of the pack. Air cooling is preferred for these systems due to the lower cost. In an air-cooled pack, the lithium-ion cells are sandwiched and packed together with spacers in-between to allow for airflow [22]. This arrangement results in complex distribution of airflow between the cells, which makes the thermal parameterization of these packs harder. Here, we consider a fixture which reproduces conditions for a portion of the cells in the pack. Therefore, it is possible to capture the cooling conditions at the face of a cell accurately in controlled conditions. By instrumenting the cell with thin film resistance temperature detector (RTD) sensors across its surface, and utilizing both an ECM and an FEM, the airflow across the cell can be identified by matching the experimental and

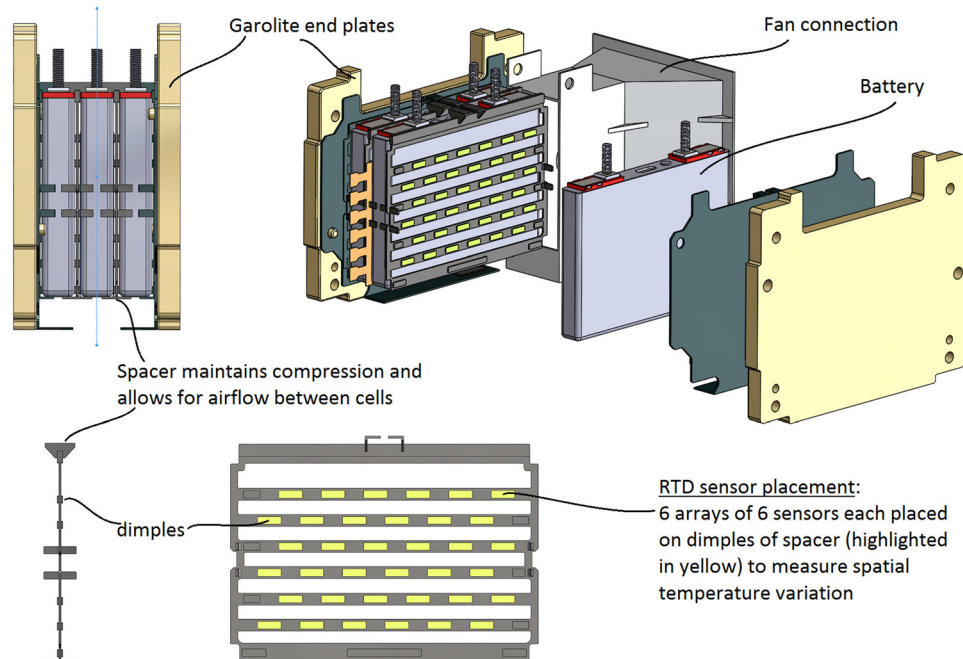


**Fig. 1 Three-cell fixture used in experiments showing placement of RTD sensors on spacer**

simulated surface temperature profiles. The methodology to achieve this goal is presented in Secs. 2.1 and 2.2. The details of the fixture used in the experiments are shown in Sec. 2.1. The cell models are explained in Sec. 2.2, which include a cell electrothermal model (ETM) and an finite element analysis model, that is, coupled to the ETM for easier airflow parameterization. Then, the results and validation data are shown in Sec. 3. Finally, the conclusion is shown in Sec. 4.

**2.1 Experimental Conditions.** A fixture is designed to replicate battery conditions associated with the cooling from the airflow on the face of a cell as shown in Fig. 1. The fixture consists of three lithium nickel–manganese–cobalt (NMC) oxide battery cells clamped together between two Garolite end plates. Each battery cell is  $120 \times 85 \times 12.7 \text{ mm}^3$  and has a nominal  $Q_{\text{nominal}} = 5 \text{ Ah}$  capacity. The cell has a (min/max/nominal) voltages of (2.9/4.1/3.7) V. A spacer is sandwiched between the batteries. The spacer has dimples which allow for airflow between the cells and maintains the compression of the fixture (refer Fig. 1). The middle battery is instrumented with an array of RTD sensors on both sides. There are 36 RTDs on each side of the battery. These thin film RTD sensors are mounted on the dimples of the spacer and measure the spatial surface temperature of the middle cell. The fixture is placed in a Cincinnati Sub-Zero ZPHS16-3.5-SCT/AC environmental thermal chamber for ambient temperature control. The fixture has a fan connection to allow for flow control. The three cells with the plastic separator in between are repeated blocks of a pack. Hence, the fixture with the fan captures the cooling conditions at the face of a cell in between

the cells accurately. The cells are also compressed to similar compressions as that in the pack. This allows the cells to experience the same thermal effects they experience in a pack given that the middle cell has the same thermal and flow boundary conditions with the ones experienced in a pack. The novel thin RTD sensors allow for spatial surface temperature measurements, while the cell is operating under flow and load conditions similar to that in the vehicle. A Bitrode model FTV provides current excitation to the three cell fixture, and the three cell voltages are recorded. The data are acquired at a rate of 1 Hz.

**2.2 Coupled Electrothermal Model.** The ETM model presented here couples a  $((m+3) \times (n+4) \times 5)$  3D thermal model with an  $(m \times n)$  2D-distributed equivalent circuit electrical model. Variables  $m$  and  $n$  are user specified. The thermal model has a five-layered mesh, as shown in Fig. 2. For  $k=1$  or 5, each layer has airflow nodes. For  $k=2$  or 4, each layer has surface nodes that represent the aluminum casing of the cell. The middle layer ( $k=3$ ) has jelly roll nodes that lump the average properties of the roll, air gap nodes, and aluminum casing nodes (edge nodes). The 2D electrical model only represents the core nodes of the jelly roll. All  $(m \times n)$  jelly roll core nodes are thus electrically and thermally connected. The electrical model generates output of terminal voltage, SOC, and heat generation. The heat generation feeds into the thermal model to determine the temperature distributions which then feed back into the electrical model to determine the electrical properties which are functions of temperature.

**2.2.1 Electrical Model.** In order to simulate the SOC and current variation at different spatial locations of the battery, a double

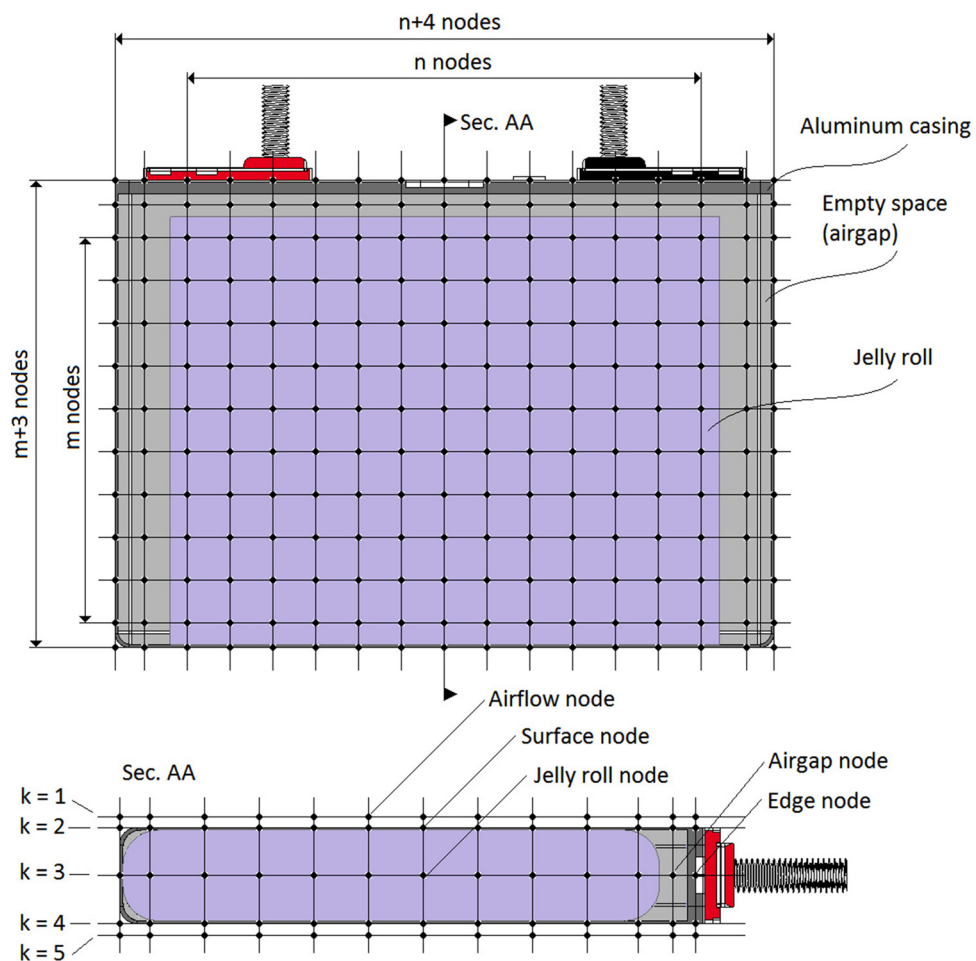
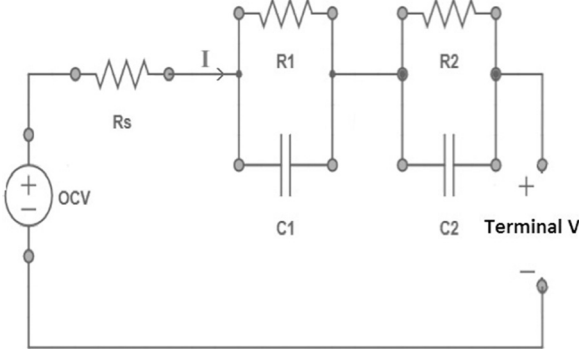


Fig. 2 Five-layered mesh for the thermal model



**Fig. 3 Double RC model representing an electrical node**

RC model is implemented at each electrical node. Figure 3 shows a schematic of the equivalent circuit model at electrical node  $(i, j)$ , where  $2 \leq i \leq m + 1$  and  $3 \leq j \leq n + 2$ , and  $n$  and  $m$  is the number of discretizations along the length and width of the jelly roll. The series resistance  $R_{s,ij}$  represents the internal resistance of the electrical node, which accounts for ohmic losses. The pairs  $(R_{1,ij}, C_{1,ij})$  and  $(R_{2,ij}, C_{2,ij})$  represent the resistances and capacitances that account for lithium diffusion in the solid and electrolyte. The OCV, which represents the open circuit voltage of the cell with no applied current, is a function of state of charge. Since the model assumes that the current collectors are infinitely conductive, this means that all electrical nodes are connected in parallel. The model at this stage does not account for tabbing. Tabs in a lithium ion cell typically have higher current densities (current/area) and hence generate more heat [23]. In the NMC cells being used, the wound jelly roll inside the encased aluminum shell of the battery is clamped at the sides by the tabs [22]. In this counter electrode tabbed configuration, the nonuniformity in current density is minimized [24]. At this point, the model neglects the non-uniformity of the current at the tabbing areas. At each  $(m \times n)$  2D spatial electrical node, a double RC equivalent circuit model is used to determine the local through-plane current density

$$\sum_{\substack{2 \leq i \leq m+1 \\ 3 \leq j \leq n+2}} I_{ij} = I \quad (1)$$

where  $I$  is the total current into the battery. At each electrical node, Kirchhoff's voltage law applies so that at node  $(i, j)$ , the following is obtained:

$$OCV_{ij} - I_{ij}R_{s,ij} - V_{1,ij} - V_{2,ij} = V_t \quad (2)$$

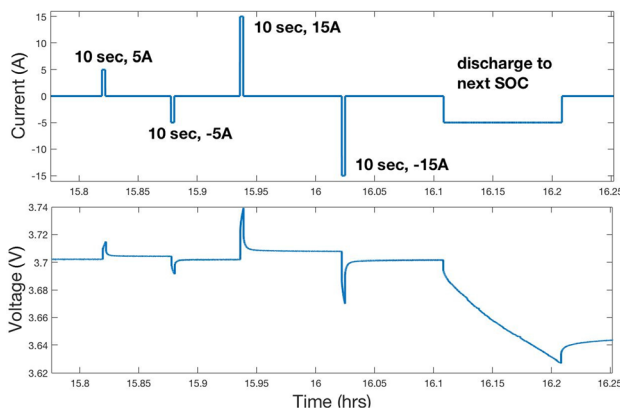


**Fig. 4 Current profile used for electrical parameterization**

So for a given input  $I$ , since  $V_{1,ij}$ ,  $V_{2,ij}$ , and  $OCV_{ij}$  are states in this model, the following equation can be solved to get the local distributions of  $I_{ij}$ :

$$\begin{bmatrix} 1 & 1 & \dots & 1 & 0 \\ R_{s,11} & 0 & \dots & 0 & 1 \\ 0 & R_{s,21} & \dots & 0 & 1 \\ \vdots & \vdots & \vdots & \vdots & \vdots \\ 0 & 0 & \dots & R_{s,mn} & 1 \end{bmatrix} \begin{bmatrix} I_{11} \\ I_{21} \\ I_{31} \\ \vdots \\ V_t \end{bmatrix} = \begin{bmatrix} I \\ OCV_{11} - V_{1,11} - V_{2,11} \\ OCV_{21} - V_{1,21} - V_{2,21} \\ \vdots \\ OCV_{mn} - V_{1,mn} - V_{2,mn} \end{bmatrix} \quad (3)$$

The state equations representing an electrical node  $(i, j)$  are:

$$\begin{bmatrix} \dot{V}_{1,ij} \\ \dot{V}_{2,ij} \\ \dot{z}_{ij} \end{bmatrix} = \begin{bmatrix} -\frac{1}{R_{1,ij}C_{1,ij}} & 0 & 0 \\ 0 & -\frac{1}{R_{2,ij}C_{2,ij}} & 0 \\ 0 & 0 & 0 \end{bmatrix} \begin{bmatrix} V_{1,ij} \\ V_{2,ij} \\ z_{ij} \end{bmatrix} + \begin{bmatrix} \frac{1}{C_{1,ij}} \\ \frac{1}{C_{2,ij}} \\ -\frac{1}{Q_{ij}} \end{bmatrix} [I_{ij}] \quad (4)$$

where  $Q_{ij} = (Q/(m \times n))$  is the nominal capacity of the cell node, and  $z_{ij}$  is the state of charge of the cell node.

**2.2.2 Thermal Model.** A 3D thermal model is also implemented where a five-layered user-defined mesh is introduced as shown in Fig. 2. The middle layer represents the thermal core nodes. The second and fourth layers are surface nodes that represent the aluminum casing. The outer most layers represent the airflow nodes. The thermal properties of aluminum are used for the surface nodes corresponding to the battery casing. The casing has a measured thickness of 0.6 mm. Air gaps exist between the jelly roll and the aluminum casing. These gaps are modeled using air thermal properties. This simplified model, where a 2D mesh is used to lump the average properties of the jelly roll, is shown to be sufficiently accurate but much faster than a detailed model [17]. Heat generation occurs at the jelly roll core nodes, and surface convection occurs at the surface nodes. Conduction in the jelly roll is assumed to be anisotropic as the thermal conductivities across the  $x-y$  plane and  $z$ -axis are an order of magnitude different as reported in Refs. [21] and [25]. Moreover, since the aluminum shell is relatively thin compared to the jelly roll, the heat conduction from the core nodes to the surface nodes is dictated only by the thermal conductivity of the jelly roll in the  $z$ -axis.

The 3D heat transfer in each thermal node  $(i, j, k)$  in the cell is governed by the general heat equation (Eq. (5))

$$\rho cV \frac{dT_{ijk}}{dt} = \dot{Q}_{gn,ijk} + \Delta Q_{ijk}, \quad \begin{array}{l} 1 \leq k \leq 5, \\ 1 \leq i \leq m+3 \\ 1 \leq j \leq n+4 \end{array} \quad (5)$$

where  $(i, j, k)$  are the coordinates of the thermal node according to the thermal mesh layout in Fig. 2. The density,  $\rho$ , is the density of the node volume,  $c$  is the specific heat capacity, and  $V$  is the volume of that node.  $\dot{Q}_{gn,ijk}$  represents the heat generation in the unit volume. Note that the heat generation only occurs in the electrical core nodes (for which  $k=3$ ). Accordingly, the heat generation  $\dot{Q}_{gn,ijk}$

---


$$\dot{Q}_{gn,ijk} = \begin{cases} I_{ij}^2 R_{s,ij} + \frac{V_{1,ij}^2}{R_{1,ij}} + \frac{V_{2,ij}^2}{R_{2,ij}} + I_{ij} T_{ij} \frac{dU}{dT} & k = 3, 2 \leq i \leq m+1, 3 \leq j \leq n+2 \\ 0 & \text{otherwise} \end{cases} \quad (6)$$

where the first three terms of Eq. (6) represent the ohmic heat generation, and the last term represents the entropic heat generation.

The heat transfer,  $\Delta Q_{ijk}$ , in Eq. (5) represents the net heat conduction in the core nodes ( $k=3$ ), or surface convection on the surface of the cell ( $k=2$  or  $k=4$ ), or the heat transfer in the air ( $k=1$  or  $k=5$ ), as shown below

$$\Delta Q_{ijk} = \begin{cases} h_{\text{surf}} A_{\text{surf}} (T_{ij(k+1)} - T_{ijk}) + (\rho c)_{\text{air}} A_{\text{gap}} v (T_{i(j-1)k} - T_{ijk}) & k = 1 \\ \frac{K_x A_x}{L_x} (T_{(i-1)jk} + T_{(i+1)jk} - 2T_{ijk}) + \frac{K_y A_y}{L_y} (T_{i(j-1)k} + T_{i(j+1)k} - 2T_{ijk}) \\ + \frac{K_z A_z}{L_z} (T_{ij(k+1)} - T_{ijk}) + h_{\text{surf}} A_{\text{surf}} (T_{ij(k-1)} - T_{ijk}) & k = 2 \\ \frac{K_x A_x}{L_x} (T_{(i-1)jk} + T_{(i+1)jk} - 2T_{ijk}) + \frac{K_y A_y}{L_y} (T_{i(j-1)k} + T_{i(j+1)k} - 2T_{ijk}) \\ + \frac{K_z A_z}{L_z} (T_{ij(k-1)} + T_{ij(k+1)} - 2T_{ijk}) & k = 3 \\ \frac{K_x A_x}{L_x} (T_{(i-1)jk} + T_{(i+1)jk} - 2T_{ijk}) + \frac{K_y A_y}{L_y} (T_{i(j-1)k} + T_{i(j+1)k} - 2T_{ijk}) \\ + \frac{K_z A_z}{L_z} (T_{ij(k-1)} - T_{ijk}) + h_{\text{surf}} A_{\text{surf}} (T_{ij(k+1)} - T_{ijk}) & k = 4 \\ h_{\text{surf}} A_{\text{surf}} (T_{ij(k-1)} - T_{ijk}) + (\rho c)_{\text{air}} A_{\text{gap}} v (T_{i(j-1)k} - T_{ijk}) & k = 5 \end{cases} \quad (7)$$


---

In the jelly roll, thermal conductivity is anisotropic. It is the same in the  $xy$ -plane, so  $K_x = K_y = K_{xy}$ , and  $K_z$  is the thermal conductivity across the electrode planes. For the air gap nodes, thermal conductivity is the same ( $K_x = K_y = K_z = K_{\text{air}}$ ).

In Eq. (7),  $A_x$ ,  $A_y$ , and  $A_z$  are the corresponding areas between neighboring nodes in the  $x$ ,  $y$ , and  $z$  directions, and they depend on the number of discretizations in the cell. Note that  $A_{\text{surf}}$ ,  $A_{\text{side}}$ , and  $A_{\text{gap}}$  are special cases of  $A_x$ ,  $A_y$ , or  $A_z$  for the cases where the node is on the surface, side, or air, respectively.  $L_x$ ,  $L_y$ , and  $L_z$  are the corresponding lengths between neighboring nodes in the  $x$ ,  $y$ , and  $z$  directions.  $T_{ijk}$  is the temperature of node  $(i, j, k)$ ,  $h_{\text{surf}}$  and  $h_{\text{side}}$  are the heat transfer coefficients along the surface and the sides of the cell, respectively, and  $v$  is the mean velocity of air over the surface of the cell, which is not measured in the experiments. This velocity will be parameterized by coupling the cell electrothermal model with a finite element flow model which will be explained in Sec. 2.2.4. Note that the radiative heat transfer could contribute up to 63% of the overall heat transfer out of the cell [17], but in this experiment, the cells are enclosed in a fixture as shown in Fig. 1, which limits the radiative heat transfer considerably. Thus,  $h_{\text{surf}}$  would be representative of the heat transfer coefficient over the surface of the battery. Finally, for those nodes that are on the sides (not the surface), another heat transfer coefficient  $h_{\text{side}}$  is considered since the conditions on the surface and the sides of the battery are different. Note that  $h_{\text{surf}}$  and  $h_{\text{side}}$  are a function of flow conditions, and are constant for a given flow condition.

**2.2.3 Electrical Model Parameterization.** The distributed model requires that electrical parameters can be identified at each node of the jelly roll. To achieve this, one double RC model was assumed to represent the entire jelly roll. Electrical parameterization was done under controlled conditions at different temperatures and SOC to characterize the resistances ( $R_s, R_1, R_2$ ) and

capacitances ( $C_1, C_2$ ) of the double RC model. This model is then expanded into a distributed model by distributing the electrical resistances ( $R_s, R_1, R_2$ ) in parallel (i.e.,  $\sum_{2 \leq i \leq m+1} (1/R_{s,ij}) = (1/R_s)$ ) among the electrical core nodes.  $\sum_{3 \leq j \leq n+2}$

Accordingly, to maintain the time constant, the capacitances ( $C_1, C_2$ ) are distributed in series (i.e.,  $\sum_{2 \leq i \leq m+1} C_{1,ij} = C_1$ ). This  $\sum_{3 \leq j \leq n+2}$

agrees with the assumption in Sec. 2.2.1 that the terminal voltage across all core nodes is the same, and that the distributed double RC circuits are assumed to be in parallel. Also, the capacity of each node is assumed to scale with the corresponding number of electrical nodes (i.e.,  $Q_{ij} = (Q_{\text{nominal}} / (m \times n))$ ). The surface nodes are only represented by thermal nodes and are thus not accounted for in the distributed double RC model.

Figure 4 shows the current profile used for parameterization at each SOC step along with the voltage profile. The battery was charged to 100% SOC and allowed to relax, and then a series of pulses were performed at different SOC. Since the electrical parameters are a function of SOC and temperature, it is important that the pulses do not result in large changes in SOC or large changes in temperatures as this will affect the accuracy of these parameters. Thus, the pulses consisted of a (5 Å, -5 Å, 15 Å, 15 Å) pulses of 10 s duration with 200 s rest after the (5 Å, -5 Å) pulses and 300 s rest after the (15 Å, -15 Å) pulses. This parameterization was done for  $T \in \{45, 35, 25, 15, 5, -5\}$  °C. A fine parameterization was done at higher and lower SOC (SOC  $\in \{0, 2.5, 5, 7.5, 10, 15, 20, 30, \dots, 80, 85, 90, 92.5, 95, 97.5, 100\}$ ) since a bigger change in the electrical parameters is expected at those SOC.

Figure 5 shows the voltage fit on the relaxation data after the -5 Å, 10 s constant current (CC) discharge pulse, and the error on the fit for three models: single, double, and triple RC models, at three different SOC (30%, 50%, and 70%). The error on voltage

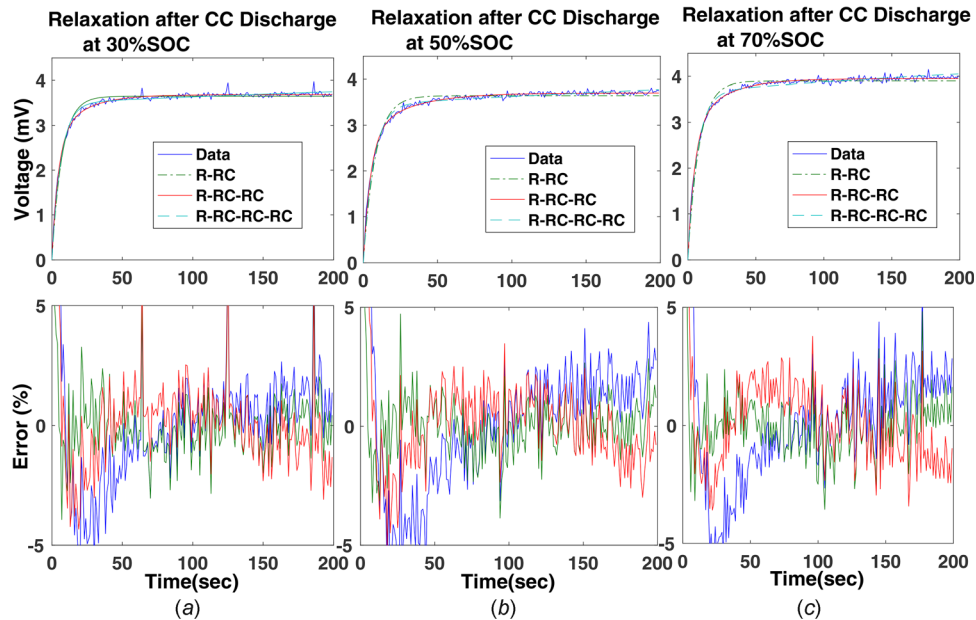


Fig. 5 Voltage fit and error for single, double, and triple RC models at: (a) 30% SOC, (b) 50% SOC, (c) 70% SOC at 25 °C, and using 5A current pulse

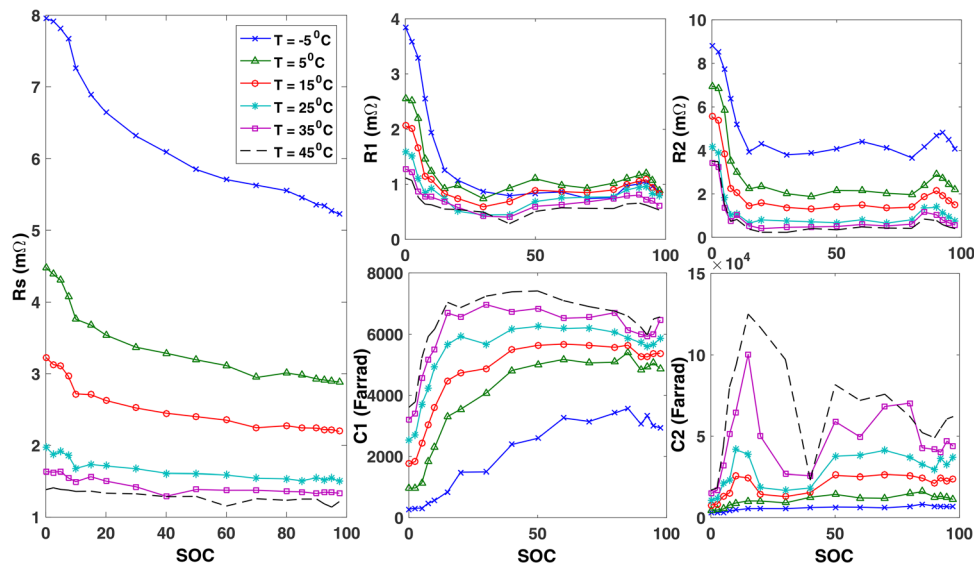


Fig. 6 Electrical parameters  $R_s$ ,  $R_1$ ,  $C_1$ ,  $R_2$ , and  $C_2$  as a function of SOC and temperature

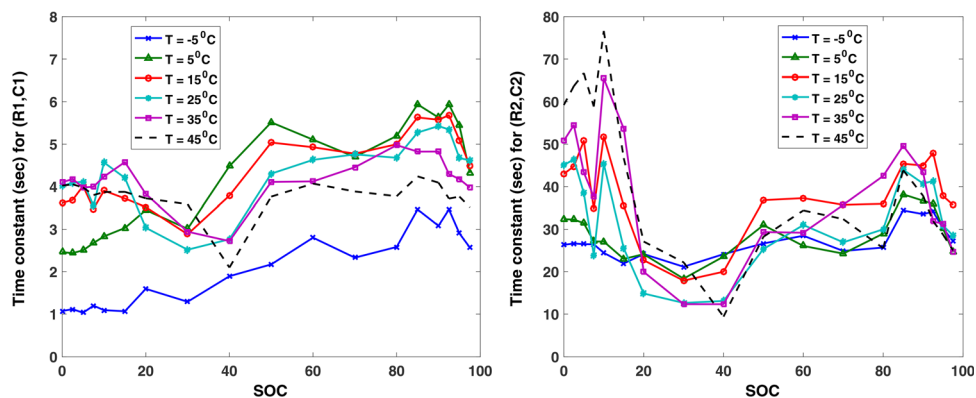
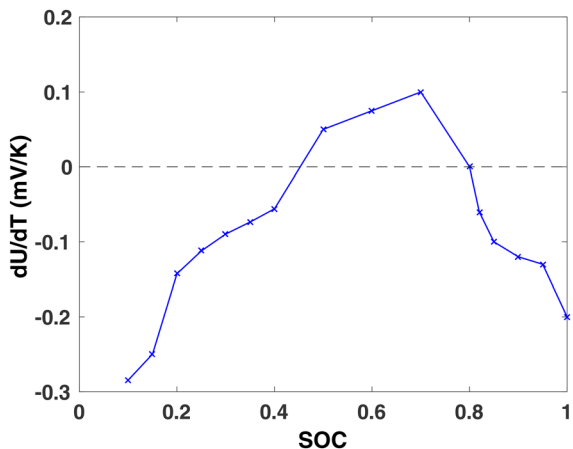


Fig. 7 Time constants for both RC pairs at different temperatures



**Fig. 8 Entropy slope  $dU/dT$  as a function of SOC as measured during discharge at  $25^{\circ}\text{C}$**

**Table 1 Thermal parameters to be identified**

Parameter	Parameterizing software
$K_{xy}$ ( $\text{W}/(\text{m}^2 \text{K})$ )	ETM
$K_z$ ( $\text{W}/(\text{m}^2 \text{K})$ )	ETM
$h_{\text{surf}}$ ( $\text{W}/(\text{m} \text{K})$ )	ETM
$h_{\text{side}}$ ( $\text{W}/(\text{m} \text{K})$ )	ETM
$(\rho c)$ ( $\text{J}/(\text{m}^3 \text{K})$ )	ETM
$v$ ( $\text{m}/\text{s}$ )	FEM

relaxation using the single RC model is larger than 5%. Using a double or triple RC model yields errors less than 5% on the voltage fit. The parameters identified using a double RC model can easily span the wide ranges of SOC and temperature and provide accurate results [12,26] and involve less state computation than the triple RC model. The resulting electrical parameters are plotted in Fig. 6. As expected, the electrical resistances decrease with increasing temperature and increase at lower SOC. The behavior of  $R_s$  as a function of temperature seems to follow an Arrhenius relationship, where the resistance increases exponentially as a function of decreasing temperature.

Figure 7 shows the time constants for the double RC pairs ( $R_1, C_1$ ) and ( $R_2, C_2$ ) at different temperatures. The electrical response of the battery has two time constants that are an order of magnitude different. The larger time constant also shows that the battery relaxes slower at lower and higher SOC.

Finally, the entropic heat generation of the battery ( $dU/dT$ ) in Eq. (6) has to be parameterized. A voltage relaxation method was used [27]. The method consists of charging or discharging the battery to a certain SOC, letting it relax, and then, changing the temperature to measure the OCV change. A step change of temperature of  $T = \{5, 15, 25, 35, 45\}^{\circ}\text{C}$  was applied, and the resulting linear fit on OCV versus  $T$  at a certain SOC was reported as the ( $dU/dT$ ) at that SOC. It is defined as

$$\frac{dU}{dT} = \frac{U(T_2) - U(T_1)}{T_2 - T_1} \quad (8)$$

where  $T$  is the temperature of the battery cell, and  $U(T)$  is the value of the OCV at that temperature. Figure 8 shows the slope ( $dU/dT$ ) at different SOC. In a lithium cobalt oxide cell, ( $dU/dT$ ) is a strong function of SOC and not temperature [18], so in this paper, entropy change is also assumed to be a function of SOC only. Thus, this experiment was performed at  $25^{\circ}\text{C}$ , and the results are considered representative of the range of temperatures in our experiments. Depending on the sign of current and ( $dU/dT$ ),

the value of  $IT(dU/dT)$  could be positive or negative implying an exothermic or endothermic reaction, respectively. This effect would be observable at low charge or discharge rates where the ohmic heat generation is small compared to the entropic heat generation. At values of SOC between 45% SOC and 80% SOC, the entropy coefficient is positive, but it is negative beyond these points.

The electrical parameters are applied at every jelly roll node in the cell. These parameters are the function of SOC and temperature. Since each node operates at a slightly different temperature, then each node will electrically operate at a slightly different SOC state.

**2.2.4 Thermal Model Parameterization.** As noted earlier in Sec. 2.2.2, the thermal jelly roll and airflow parameters of the battery are unknown. These parameters are shown in Table 1 below along with which model they are being identified with. Many papers have cited values for the thermal parameters [13,21,25], but in our case, since each core node in the jelly roll is considered a lumped node, parameterization was done to quantify the values of these lumped parameters.

The thermal parameterization was performed in two steps:

- **Step 1:** An optimization fitting algorithm was applied to identify the first five parameters in Table 1 under a simple natural convection scheme with no airflow. Since it is a natural convection scheme, the velocity term,  $v$ , was dropped in Eq. (7). This allowed for the identification of parameters  $K_{xy}$ ,  $K_z$ ,  $h_{\text{surf}}$ ,  $h_{\text{side}}$ , and  $\rho c$ . Note that parameters  $K_{xy}$ ,  $K_z$ ,  $h_{\text{side}}$ , and  $\rho c$  are independent of the air flow. Only  $h_{\text{surf}}$  and the flow velocity,  $v$ , over the surface of the cell would change as the convection conditions change. These would be identified by coupling with the FEM.

- **Step 2:** This step is implemented offline. The objective of this step is to identify the mean air flow velocity,  $v$ , over the surface of the cell. A forced convection scheme was considered, where moving air was present to cool the battery. Air flow was produced by a cooling fan that was attached to the three-cell fixture air outlet (refer Fig. 1). Parameters  $K_{xy}$ ,  $K_z$ ,  $h_{\text{side}}$ , and  $\rho c$  were assumed unchanged and were fed to a FEM. The airflow parameter,  $v$ , was parameterized by using a training data set (39 Å pulsing under forced natural convection). This identified value of  $v$  was also validated using the FEM against two other experiments (20 Å and 50 Å under the same forced laminar convection scheme). The resulting velocity,  $v$ , was then fed back into the equivalent circuit model, where the heat transfer coefficient,  $h_{\text{surf}}$ , was tuned under the same forced convection scheme used in the FEM (i.e., using the same velocity and pulsing profiles). The flow chart shown in Fig. 9 shows the process of cascading the parameterization between the FEM and the equivalent circuit model.

#### Step 1: Parameter Fitting

The least squares method was used to identify the parameters in the ECM under natural convection cooling conditions [12]. Thermal Eqs. (5) through (7) were solved using ODE solver in MATLAB, and the resulting simulated surface temperature distributions were interpolated into the 36 RTD sensor locations shown in Fig. 1. A least squares was performed on all  $n = 1, \dots, 36$  RTD sensors for the duration of the simulation,  $t \in [0, 120,000]$  s, to find the best fit for the parameters. The objective function  $J$  to minimize is

$$J = \sum_{n=1}^{36} \sqrt{\sum_{t=0}^{t_{\text{end}}} (\bar{T}_n(t) - T_n(t))^2} \quad (9)$$

where  $\bar{T}_n(t)$  and  $T_n(t)$  are the measured and simulated temperatures, respectively, at the sensor locations at time  $t$ . Appropriate scaling of the parameters and normalization of the temperature

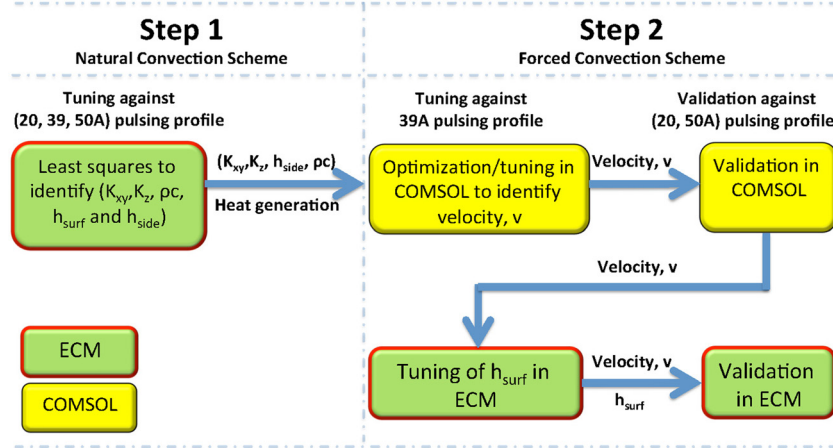


**Fig. 9** Flowchart showing the process of cascading parameterization in comsol

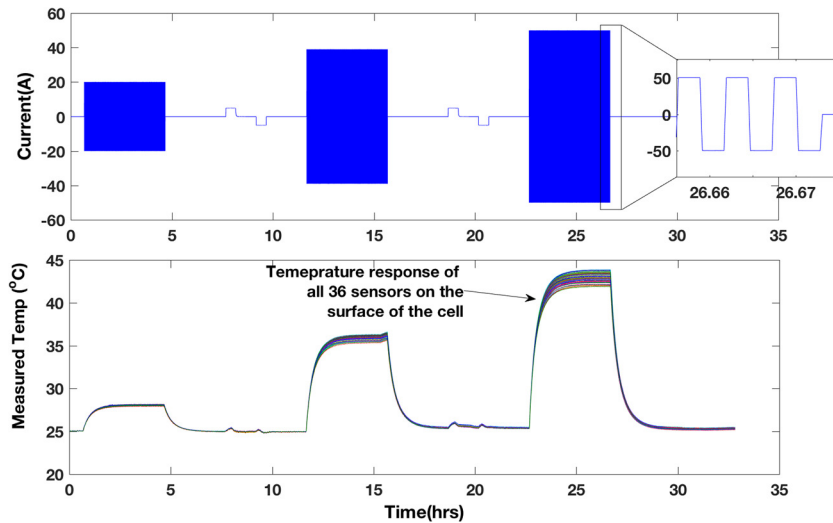


**Fig. 10** Current profile used for thermal parameterization at 25 °C and the corresponding measured surface temperatures

error could improve the convergence of the minimization problem but these numerical issues were not pursued.

Figure 10 shows the current profile used for parameterization and the corresponding measured temperatures on the surface of the battery from all 36 sensors. The experiment is performed under natural convection schemes where the fixture fan is turned off, and the chamber fan is turned on to maintain ambient temperature. This meant that there was no airflow over the surface and the only parameters to identify were the thermal conductivities ( $K_{xy}$ ,  $K_z$ ), heat transfer coefficients ( $h_{surf}$  and  $h_{side}$ ) and  $\rho c$ . The parameters  $K_{xy}$ ,  $K_z$ ,  $\rho c$ , and  $h_{side}$  are independent of the convection scheme. Parameter  $h_{surf}$  is reparameterized in step 2 along with

the airflow velocity since it depends on the convection scheme. Multiple current pulses with amplitudes of 20 Å, 39 Å, and 50 Å were used to ensure sufficient excitation. The pulses had a width of 20 s each and were applied to the battery after discharging to

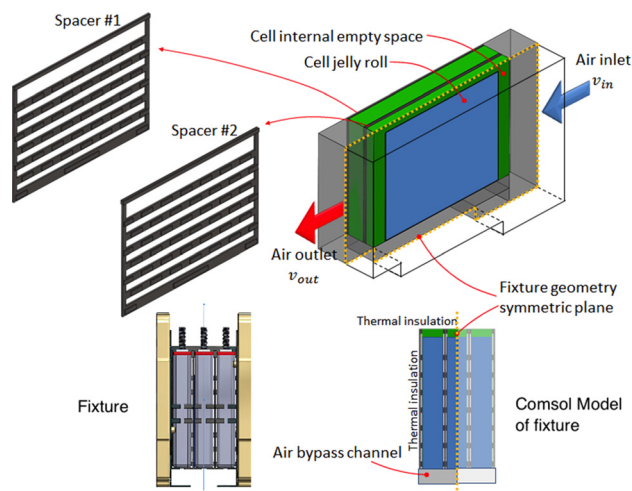


**Fig. 11** Three-dimensional FEM of the three-cell fixture

50%SOC and allowing sufficient time for the temperature and voltage to relax and equilibrate with the chamber temperature. Each excitation was applied for 4 h to allow for thermal equilibrium as shown in Fig. 10.

The values of the parameters that resulted from the thermal parameterization under a natural convection scheme are shown in Table 2 (in bold) along with the thermal parameters of aluminum and air.

In a forced convection scheme, the airflow velocity  $v$  is not measured. Both  $v$  and  $h_{\text{surf}}$  would have to be parameterized since different airflow velocities result in different heat transfer coefficients. Parameters  $K_{xy}$ ,  $K_z$ ,  $\rho c$ , and  $h_{\text{side}}$  would remain unchanged since they are independent of the flow conditions. One could deduce the heat transfer coefficient  $h_{\text{surf}}$  from the airflow velocity given the heat transfer relations provided in the literature for flow over flat plates [28]. However, in this case, the complex geometry of the flow area between the cells due to the spacer would result in a heat transfer coefficient, that is, different from what could be deduced from the literature relations. As such, to parameterize  $v$  and  $h_{\text{surf}}$ , the authors reverted to coupling the parameterization with a FEM and characterize the heat transfer coefficient as a function of different flow rates. At this stage, though, only one flow rate condition was used and validated against.

#### Step 2: Finite Element Model Coupling

In this step, a finite-element model was implemented to identify the air flow velocity,  $v$ , produced by the cooling fan. The  $K_{xy}$ ,  $K_z$ ,  $h_{\text{side}}$ , and  $\rho c$  identified in step 1 were assumed unchanged and were assigned to the finite-element model. The 20 Å, 39 Å, and 50 Å excitation currents shown in Fig. 4 were applied under a forced convection scheme with constant fan speed. The mean air flow velocity,  $v$ , was identified first using the 39 Å pulsing experiment as the training date set. Then, the 20 Å and 50 Å pulsing experiments were used for validation. The identified  $v$  was then fed into Eq. (7) for the parameter identification of the corresponding  $h_{\text{surf}}$  in the electrothermal model.

The FEM setup is illustrated in Fig. 11. The battery cell is composed of the jelly roll and the outside aluminum casing. The 0.6-mm thick aluminum casing was modeled using a thin conductive layer, which is a boundary coupling feature in COMSOL software environment. Therefore, the aluminum casing is not physically drawn in Fig. 11. The jelly roll touches the aluminum casing on the side and bottom, leaving an internal empty space in the cell. This empty space is filled with air and small amounts of electrolyte. The electrolyte was neglected in the finite element analysis for simplicity. The entire fixture has three-cells and four spacers, forming a symmetric geometry with the symmetric plane splitting the middle cell as shown in Fig. 11. Therefore, only half of the geometry is necessary for finite element analysis. The symmetric

plane is marked by the yellow dotted line. The spacers create air path over the cell side surfaces for cooling. The cells and the spacers were clamped together using two Garolite blocks, which were not physically modeled in 3D but were mathematically modeled as thermal insulation boundary condition due to its low thermal conductivity. The top surfaces of the cells were mostly covered by plastic terminal blocks and were also modeled as thermal insulation. The cooling fan was modeled by uniform normal air flow velocity on the outlet boundary. Air at ambient temperature enters the fixture through the air inlet and exits the fixture through the outlet at a higher temperature. In addition, the fixture setup allows a portion of the cooling air to go through a bypass channel under the cells and then enter the space between the cells from the bottom.

The whole geometry was meshed with free tetrahedral structure at element sizes between 1 and 4.5 mm. This is sufficient to maintain good element quality for the 2.4 mm spacer between cells. Conjugated heat transfer solver module was used to compute the air dynamics together with heat convection and conduction. Navier-Stokes equations for compressible fluid were used to model the air flow.

Since the FEM results in air flow velocity over the surface of the cell, that is, nonuniform due to the complex geometry of the dimples of the spacer, the outlet velocity,  $v_{\text{out}}$ , at the air outlet (refer Fig. 11) was used in the tuning process. The mean air flow velocity,  $v$ , which will be used in the electrothermal model, could then be approximated using Eq. (10).

$$\frac{v_{\text{out}}}{v} = \frac{A_{\text{out}}}{A_{\text{cells}}} \quad (10)$$

where  $A_{\text{out}}$  is the air outlet surface area, and  $A_{\text{cells}}$  is the area of airflow between the cells. In this approximation, air is assumed incompressible.

The iterative process of tuning  $v_{\text{out}}$  consisted of minimizing the error,  $E$ , between the cell surface temperature measurements and COMSOL simulation results at the surface sensor locations, which

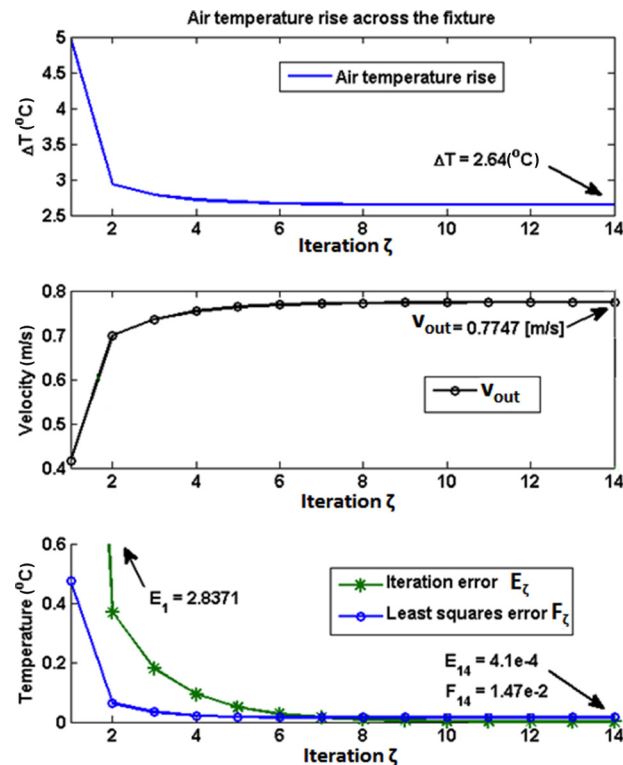


Fig. 13 Numerical model parameterization process using the optimization logic defined in Eq. (11)

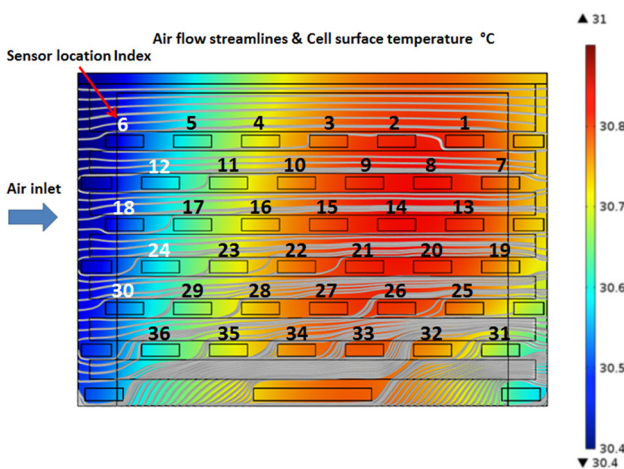


Fig. 12 Location of the sensors on the surface of the cell and the cell surface temperature distribution for 39 Å cycling case

are marked in Fig. 12. Also shown in Fig. 12 are the streamlines of airflow over the surface of the cell.

Due to the fact that the surface temperature decreases as flow rate  $v_{\text{out}}$  increases, the optimization logic was defined by Eq. (11)

$$v_{\text{out}}(\zeta + 1) = v_{\text{out}}(\zeta) - dE(\zeta) \quad (11)$$

where  $v_{\text{out}}(\zeta)$  is the outlet air flow velocity at the  $\zeta^{\text{th}}$  iteration, and  $d$  is the parameter tuning gain. The iteration error at the  $\zeta^{\text{th}}$  iteration,  $E(\zeta)$ , is defined by Eq. (12)

$$E(\zeta) = \frac{1}{36} \sum_{n=1}^{36} (\bar{T}_n - T_n(\zeta)) \quad (12)$$

where  $n$  is the sensor location index on the cell surface.  $\bar{T}_n$  and  $T_n$  are the experimental and simulated steady-state surface temperatures, respectively, at the locations of the sensors ( $n = 1, \dots, 36$ ). The optimization tuning gain,  $d$ , is adjusted for proper convergence. In this particular study,  $d = (1/10)$  was used. Note that the cost function can be normalized for improving the convergence speed for estimation  $v_{\text{out}}$ , but this study was not pursued.

For an initial guess of the air outlet velocity  $v_{\text{out},0}$ , an energy balance on the airflow control volume into and out of the fixture can be formulated using Eq. (13)

$$\dot{m}_{\text{in}} h_{\text{in}} - \dot{m}_{\text{out}} h_{\text{out}} = \dot{Q}_{\text{in}} \quad (13)$$

where  $\dot{m}_{\text{in}}$  and  $\dot{m}_{\text{out}}$  are the inlet and outlet mass flow rates into the airflow control volume and are equal, so  $\dot{m}_{\text{in}} = \dot{m}_{\text{out}} = \dot{m} = \rho A v$ . The enthalpies of the airflow in and out are  $h_{\text{in}} = c T_{\text{in}}$  and  $h_{\text{out}} = c T_{\text{out}}$ , respectively. Finally, the heat transfer into the control volume can be approximated as the heat generation from all three cells in the fixture as  $\dot{Q}_{\text{in}} = 3 \dot{Q}_{\text{cell,gn}}$ .

Thus, the initial guess of the air outlet velocity is calculated using Eq. (14) below

$$\begin{aligned} v_{\text{out},0} &= \frac{3 \dot{Q}_{\text{cell,gn}}}{(\rho c)_{\text{air}} \Delta T_0 A_{\text{outlet}}} \\ &= \frac{3 \times 2.546 \text{ W}}{1.15 \text{ kg/m}^3 \times 1000 \text{ J/kg K} \times 4 \text{ K} \times 3986.5 \text{ mm}^2} \\ &= 0.416 \text{ m/s} \end{aligned} \quad (14)$$

where  $\dot{Q}_{\text{cell,gn}}$  is the heating power of one cell at steady state when the current excitation is 39 Å. The density and heat capacity of air are  $\rho_{\text{air}}$  and  $c_{\text{air}}$ , respectively.  $\Delta T_0$  is an initial estimate of the temperature increase of the air across the fixture, which is defined as the average air temperature on the outlet minus the air inlet temperature.  $A_{\text{outlet}}$  is the fixture outlet area.

For the case considered, the fitting process and results are plotted in Fig. 13. The air temperature rise across the fixture,  $\Delta T$ , is plotted in the top graph. Decreasing  $\Delta T$  indicates the initial guess of  $v_{\text{out}}$  is lower than the true value. The outlet air flow velocity  $v_{\text{out}}$  is shown in the middle plot. In the bottom figure, the value of the optimization iteration error  $E(\zeta)$  defined in Eq. (12) is compared with the least squares error  $F(\zeta)$ , which is defined in Eq. (15)

$$F(\zeta) = \frac{1}{36} \sqrt{\sum_{n=1}^{36} (\bar{T}_n - T_n(\zeta))^2} \quad (15)$$

The final outlet air flow velocity was  $v_{\text{out}} = 0.8 \text{ m/s}$ , and was validated using the other two forced convection experimental data sets (20 Å and 50 Å current excitation). The mean flow velocity between the cells,  $v$  is then calculated using Eq. (10) and fed back into the electrothermal model. Given that parameters  $K_{xy}$ ,  $K_z$ ,  $h_{\text{side}}$ ,

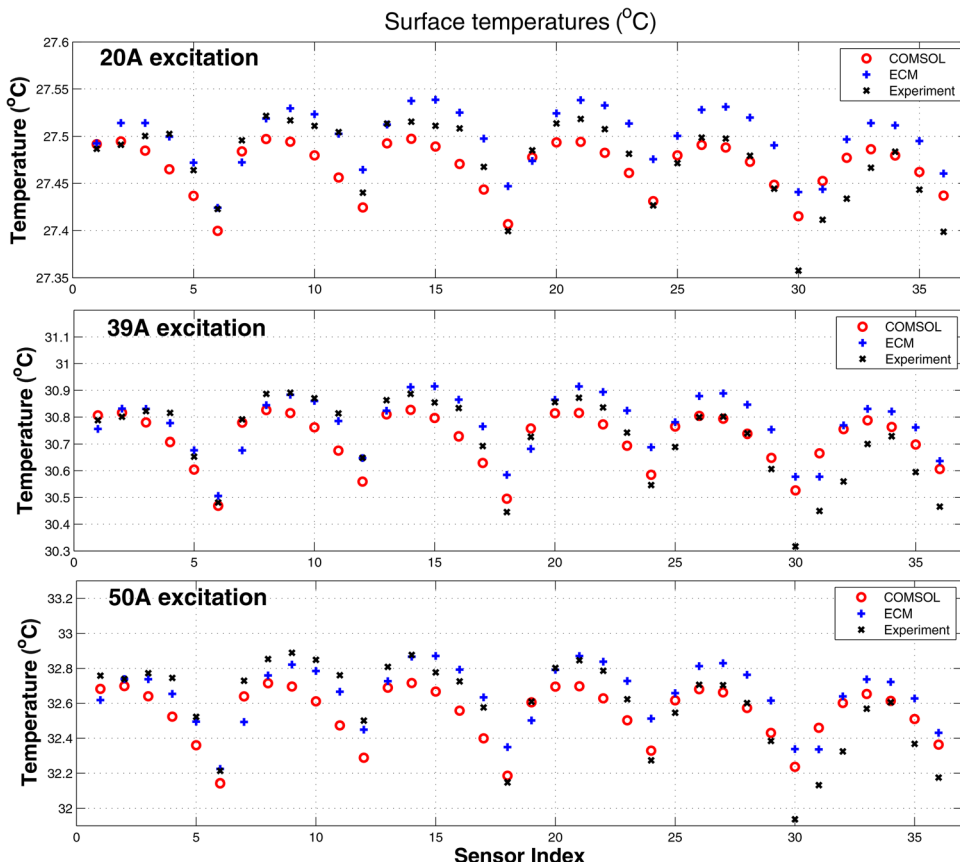
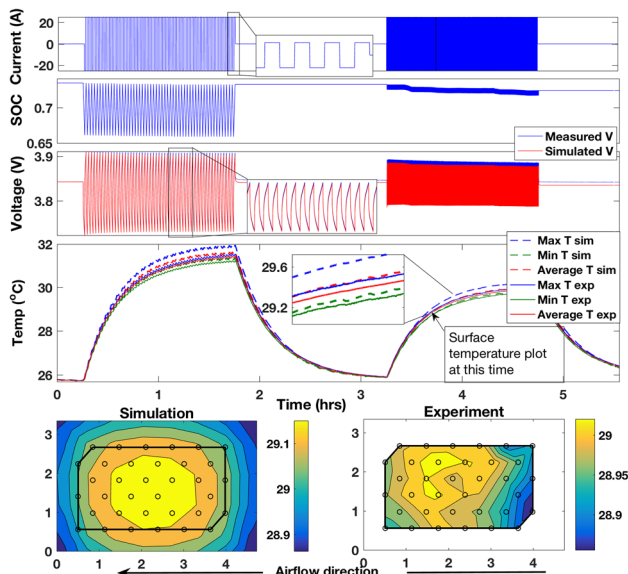


Fig. 14 Temperature rise at steady-state at the 36 sensor locations using comsol, ETM, and experimental data using a 20 Å, 39 Å, and 50 Å excitation profiles

**Table 3 Experiments used for validation of the coupled ETM**

Experiment	Temperature (°C)	Current amplitude (A)	SOC (%)	Pulse profile	$V_{RMSE}$ (mV)	$T_{max,RMSE}$ (°C)	$T_{min,RMSE}$ (°C)	$T_{avg,RMSE}$ (°C)
Pulse	25	25	50	50/5 s	5.5	0.1	0.2	0.1
Pulse	25	50	50	50/5 s	7.9	0.3	0.4	0.3
Pulse	25	25	25	50/5 s	8.6	0.1	0.2	0.1
Pulse	25	25	75	50/5 s	2.8	0.2	0.2	0.2
Pulse	10	50	50	50/5 s	8.5	0.4	0.6	0.4
Pulse	-5	50	50	50/5 s	8.8	1.3	1.8	1.3
US06	25	—	—	—	15.5	0.3	0.4	0.2
Cold FTP	-5	—	—	—	14.7	0.8	2.3	1.2
Urban assault	25	—	—	—	12.9	0.2	0.3	0.2



**Fig. 15 Pulse validation experiment at 25 °C, 75% SOC, and 25 A current amplitude**

$\rho_c$ , and  $v$  are now known, the surface heat convection coefficient,  $h_{surf}$ , is tuned against the 39 Å excitation data with forced convection. The identified  $h_{surf}$  was then validated against the other two data sets (20 Å and 50 Å) under a forced convection scheme. The temperature results from all three experiments using COMSOL and the electrothermal model along with the experimental data are illustrated in Fig. 14 at the 36 sensor locations.

### 3 Model Validation

In this section, the proposed equivalent circuit model is validated against several experiments that considered different drive cycles and pulse experiments at different temperatures, states of charge, current amplitude, and pulse width.

The model is validated and shows agreement with all experiments both electrically (terminal voltage) and thermally (surface

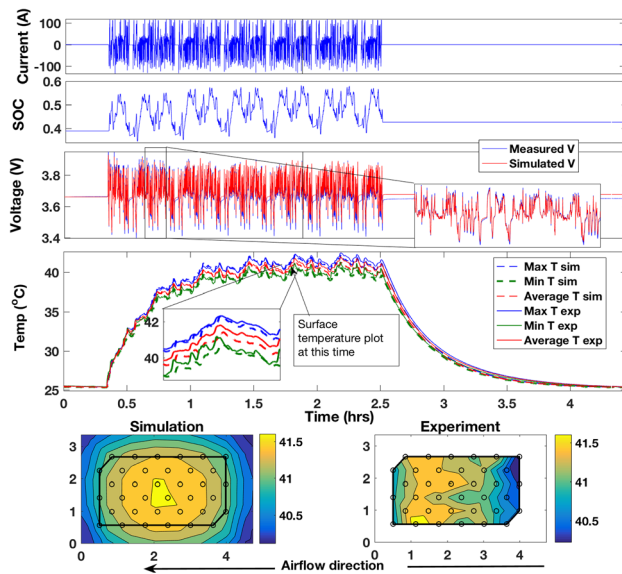


**Fig. 16 Simulated and experimental electrothermal behavior during a hybrid power split for a US06 drive cycle at 25 °C**

temperature) within the RTD sensor accuracy of 0.5 °C. Table 3 summarizes the list of experiments used for validation and the corresponding RMSE on voltage and surface temperature in each case.

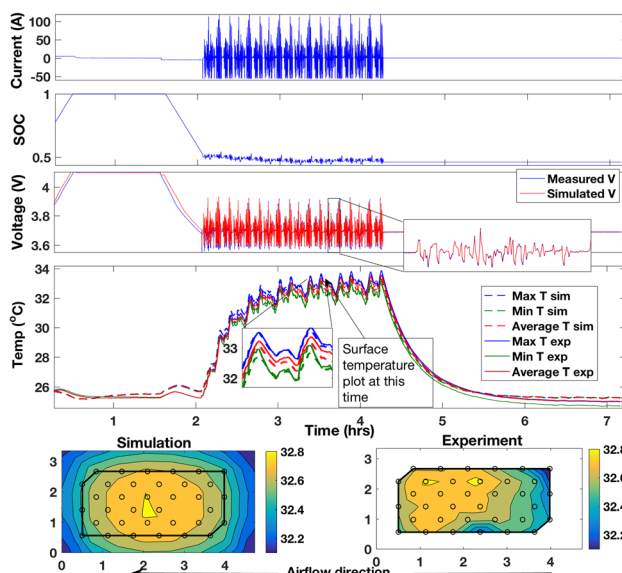


**Fig. 17 Simulated and experimental electrothermal behavior during a hybrid power split for an urban assault drive cycle 25 °C**

**Table 4 Details of the US06, FTP and urban assault cycle (UAC)**

	US06	FTP	UAC
Duration (s)	1320	1372	1233
RMS current (Å)	45	29	33
Max   current   (Å)	137	108	120
Max  Δ current   (Å)	84	143	99
Max SOC swing (%)	20	17	7

The first column in Table 3 indicates the type of experiment.

The second, third, and fourth columns indicate the temperature, SOC, and current amplitude at which the experiment was performed. Column 5, which is the pulse profile, has two entries which indicate that the first set of pulses have a width of 50 s, and the second set have 5 s.

**3.1 Pulse Excitation Experiments.** In this section, the coupled ETM is validated against pulsing experiments for varying temperatures, SOC, current amplitudes, and pulse widths. Figure 15 shows the current profile, corresponding SOC, voltage and thermal response, and a spatial temperature distribution profile for both the measured and simulated ETM data at a specified time  $t$  for a given pulsing experiment. Plots of temperature versus time show the minimum, maximum, and average (simulated and measured) surface temperature evolution. The average interior temperature is also plotted, and it shows that the difference between the average interior and average surface temperature is less than 1 °C. Although hard to spot, Fig. 15 shows the slight asymmetry in the simulated surface temperature profiles induced by the airflow. The results of pulsing experiments with different conditions (ambient temperature, nominal SOC, pulse amplitude, and width) are tabulated in Table 3. The results in Table 3 indicate that for higher current rates, the RMSE values are slightly higher than those for lower current rates. This suggests that electrical parameters could be a function of C-rate and could be parameterized accordingly. Moreover, the pulse experiment at -5 °C shows that the RMSE on voltage is 8.8 mV, which is in good agreement with the results at other pulsing experiments, but the RMSE for the minimum and maximum temperatures exceeds 1 °C. This could suggest that, at lower temperatures, the parameterized thermal properties could be different.

**3.2 Drive Cycle Validation.** Three drive cycles have been used for validation in this section. These cycles are high power cycles extracted from a hybrid electric vehicle operating on a US06, FTP, and UAC cycles. The details of the power split in the vehicle are irrelevant, but the specifics of the current profiles are shown in Table 4. The US06 drive cycle was scaled down to match the power capabilities of our battery. The ETM showed good agreement between the measured and simulated voltages and temperatures for the US06 drive cycle and the UAC shown in Figs. 16 and 17. The simulated surface temperature profiles also show the asymmetry with the hot spot shifted slightly due to the airflow. Also, note that the experimental surface temperature data shown in Figs. 16 and 17 are snapshots in time, and the locations of the hotspots in these profiles move around a bit because of the noise on the sensors. This makes it much harder to capture exactly the location of the hot spot. However, for the Cold FTP cycle the RMSE on the estimated voltage is comparable to that of the US06 cycle, but the RMSE on temperatures is higher as shown in Table 3. This agrees with what was shown earlier in Sec. 3.1 that at lower temperatures, the RMSE on temperatures is large. These observations need to be examined further to understand the effect of temperature (especially lower temperatures) on spatial temperature distributions in a prismatic lithium-ion cell.

## 4 Conclusion

A methodology for coupling the parameterization of an ECM with an FEM has been presented, which allows for the parameterization of the ECM in replicating the cooling experienced by the cells in pack conditions due to the airflow by their sides. In complex pack geometries, a seamless coupling between the ECM and the FEM can result in easier airflow parameterization. Also, the ECM developed in this study was validated against a wide range of experimental conditions. The model couples a 2D distributed double RC model network with a 3D thermal model for a lithium ion prismatic cell. The analysis considered a prismatic NMC

lithium-ion battery. The presented ECM showed good agreement with the experimental data under different experimental conditions. Validation was performed using different pulsing profiles ( $T_{amb} \in [-5, 10, 25] °C$ ,  $I \in [25, 50] A$ , SOC  $\in [25, 50, 75] %$ , and pulse width  $\in [5, 50] s$ ) and different drive cycles ( $T_{amb} \in [-5, 25] °C$ ).

This model has shown agreement with the experimental data and was able to capture the average and minimum and maximum temperatures with good accuracy. Future work will include investigating optimal sensor placement on the surface of the cell, and reducing and scaling the model to a battery pack to study the spatial temperature variations induced by airflow, and investigating optimal sensor placement on a pack level. Furthermore, the applicability of this methodology on other types of automotive pack coolants can be investigated, such as liquid coolants which are more common in battery electric vehicles and plug-in hybrid electric vehicles.

## Acknowledgment

The information, data, or work presented herein was funded in part by the Advanced Research Projects Agency-Energy (ARPA-E), U.S. Department of Energy, under Award Number DE-AR0000269. The authors would like to acknowledge the contribution of Aaron Knobloch and Christopher Kapusta from GE Global Research and Brian Engle from Amphenol Advanced Sensors for providing the RTD sensors and for their continuous feedback and support.<sup>1</sup>

## References

- [1] Mandal, B. K., Padhi, A. K., Shi, Z., Chakraborty, S., and Filler, R., 2006, "Thermal Runaway Inhibitors for Lithium Battery Electrolytes," *J. Power Sources*, **161**(2), pp. 1341–1345.
- [2] Bernardi, D., Pawlikowski, E., and Newman, J., 1985, "A General Energy Balance for Battery Systems," *J. Electrochem. Soc.*, **132**(1), pp. 5–12.
- [3] Doyle, M., Fuller, T. F., and Newman, J., 1993, "Modeling of Galvanostatic Charge and Discharge of the Lithium/Polymer/Insertion Cell," *J. Electrochem. Soc.*, **140**(6), pp. 1526–1533.
- [4] Fuller, T. F., Doyle, M., and Newman, J., 1994, "Simulation and Optimization of the Dual Lithium ion Insertion Cell," *J. Electrochem. Soc.*, **141**(1), pp. 1–10.
- [5] Safari, M., Morcrette, M., Teysset, A., and Delacourta, C., 2009, "Multimodal Physics-Based Aging Model for Life Prediction of Li-Ion Batteries," *J. Electrochem. Soc.*, **156**(3), pp. A145–A153.
- [6] Lin, X., Perez, H. E., Siegel, J. B., Stefanopoulou, A. G., Li, Y., Anderson, R. D., Ding, Y., and Castanier, M. P., 2013, "Online Parameterization of Lumped Thermal Dynamics in Cylindrical Lithium Ion Batteries for Core Temperature Estimation and Health Monitoring," *IEEE Trans. Control Syst. Technol.*, **21**(5), pp. 1745–1755.
- [7] Murashko, K., Pyrhonen, J., and Laurila, L., 2013, "Three-Dimensional Thermal Model of a Lithium Ion Battery for Hybrid Mobile Working Machines: Determination of the Model Parameters in a Pouch Cell," *IEEE Trans. Energy Convers.*, **28**(2), pp. 335–343.
- [8] Einhorn, M., Conte, F., Kral, C., and Fleig, J., 2013, "Comparison, Selection, and Parameterization of Electrical Battery Models for Automotive Applications," *IEEE Trans Power Electron.*, **28**(3), pp. 1429–1437.
- [9] Hu, Y., Yurkovich, S., Guezenec, Y., and Yurkovich, B., 2011, "Electro-Thermal Battery Model Identification for Automotive Applications," *J. Power Sources*, **196**(1), pp. 449–457.
- [10] Lam, L., Bauer, P., and Kelder, E., 2011, "A Practical Circuit-Based Model for Li-Ion Battery Cells in Electric Vehicle Applications," 2011 IEEE 33rd International Telecommunications Energy Conference (INTELEC), Oct. 9–13.
- [11] Gao, L., Liu, S., and Dougal, R., 2002, "Dynamic Lithium-Ion Battery Model for System Simulation," *IEEE Transactions on Components and Packaging Technologies*, **25**(3), pp. 495–505.

<sup>1</sup>The information, data, or work presented herein was funded in part by an agency of the United States Government. Neither the United States Government nor any agency thereof, nor any of their employees, makes any warranty, express or implied, or assumes any legal liability or responsibility for the accuracy, completeness, or usefulness of any information, apparatus, product, or process disclosed, or represents that its use would not infringe privately owned rights. Reference herein to any specific commercial product, process, or service by trade name, trademark, manufacturer, or otherwise does not necessarily constitute or imply its endorsement, recommendation, or favoring by the United States Government or any agency thereof. The views and opinions of authors expressed herein do not necessarily state or reflect those of the United States Government or any agency thereof.

- [12] Perez, H. E., Siegel, J. B., Lin, X., Ding, Y., and Castanier, M. P., 2012, "Parameterization and Validation of an Integrated Electro-Thermal LFP Battery Model," *ASME* Paper No. DSCC2012-MOVIC2012-8782.
- [13] Jung, S., and Kang, D., 2014, "Multi-Dimensional Modeling of Large-Scale Lithium-Ion Batteries," *J. Power Sources*, **248**(0), pp. 498–509.
- [14] Smith, K., Kim, G.-H., Darcy, E., and Pesaran, A., 2010, "Thermal/Electrical Modeling for Abuse-Tolerant Design of Lithium Ion Modules," *Int. J. Energy Res.*, **34**(2), pp. 204–215.
- [15] Fleckenstein, M., Bohlen, O., Roscher, M. A., and Bker, B., 2011, "Current Density and State of Charge Inhomogeneities in Li-Ion Battery Cells With Lifepo<sub>4</sub> as Cathode Material Due to Temperature Gradients," *J. Power Sources*, **196**(10), pp. 4769–4778.
- [16] Kim, Y., Mohan, S., Siegel, J. B., and Stefanopoulou, A. G., 2013, "Maximum Power Estimation of Lithium-Ion Batteries Accounting for Thermal and Electrical Constraints," *ASME* Paper No. DSCC2013-3935.
- [17] Chen, S., Wan, C., and Wang, Y., 2005, "Thermal Analysis of Lithium-Ion Batteries," *J. Power Sources*, **140**(1), pp. 111–124.
- [18] Inui, Y., Kobayashi, Y., Watanabe, Y., Watase, Y., and Kitamura, Y., 2007, "Simulation of Temperature Distribution in Cylindrical and Prismatic Lithium ion Secondary Batteries," *Energy Convers. Manage.*, **48**(7), pp. 2103–2109.
- [19] Samba, A., Omar, N., Gualous, H., Firouz, Y., den Bossche, P. V., Mierlo, J. V., and Boubekeur, T. I., 2014, "Development of an Advanced Two-Dimensional Thermal Model for Large Size Lithium-Ion Pouch Cells," *Electrochim. Acta*, **117**(0), pp. 246–254.
- [20] Gerver, R. E., and Meyers, J. P., 2011, "Three-Dimensional Modeling of Electrochemical Performance and Heat Generation of Lithium-Ion Batteries in Tabbed Planar Configurations," *J. Electrochem. Soc.*, **158**(7), pp. A835–A843.
- [21] Taheri, P., and Bahrami, M., 2012, "Temperature Rise in Prismatic Polymer Lithium-Ion Batteries: An Analytic Approach," *SAE* Paper No. 2012-01-0334.
- [22] Stefanopoulou, A. G., Mohan, S. N., Kim, Y., and Siegel, J. B., 2016, "Bulk Force in a Battery Pack and Its Application to State of Charge Estimation," *U.S. Patent No. 2016/0064972 A1*.
- [23] Peck, S., Olszanski, T., Zanardelli, S., and Pierce, M., 2012, "Validation of a Thermal-Electric Li-Ion Battery Model," *SAE Int. J. Passeng. Cars Electron. Electr. Syst.*, **5**(1), pp. 154–163.
- [24] Kim, G.-H., Smith, K., Lee, K.-J., Santhanagopalan, S., and Pesaran, A., 2011, "Multi-Domain Modeling of Lithium-Ion Batteries Encompassing Multi-Physics in Varied Length Scales," *J. Electrochem. Soc.*, **158**(8), pp. A955–A969.
- [25] Maleki, H., Hallaj, S. A., Selman, J. R., Dinwiddie, R. B., and Wang, H., 1999, "Thermal Properties of Lithium-Ion Battery and Components," *J. Electrochem. Soc.*, **146**(3), pp. 947–954.
- [26] Lin, X., Perez, H. E., Mohan, S., Siegel, J. B., Stefanopoulou, A. G., Ding, Y., and Castanier, M. P., 2014, "A Lumped-Parameter Electro-Thermal Model for Cylindrical Batteries," *J. Power Sources*, **257**, pp. 1–11.
- [27] Hallaj, S. A., Prakash, J., and Selman, J., 2000, "Characterization of Commercial Li-Ion Batteries Using Electrochemical-Calorimetric Measurements," *J. Power Sources*, **87**(1), pp. 186–194.
- [28] Incropera, F., 2007, *Fundamentals of Heat and Mass Transfer*, Wiley, Hoboken, NJ.